

# Radio over Fiber with Cascaded Structure: Algorithm for Uplink Positioning

Dexin Kong, *Student Member, IEEE*, Diana Pamela Moya Osorio, *Member, IEEE*, and Erik G. Larsson, *Fellow, IEEE*

**Abstract**—Recent advancements in polymer microwave fiber (PMF) technology have created significant opportunities for robust, low-cost, and high-speed sub-terahertz (THz) radio-over-fiber communications. Recognizing these potential benefits, this paper explores a novel radio-over-fiber (RoF) structure that interconnects multiple radio units (RUs) in cascade via fiber, envisioning its application in indoor scenarios. This structure creates a number of research opportunities when considering cascaded distortion effects introduced by non-linear power amplifiers (PAs) at the RUs and the propagation channel over the fiber.

We propose maximum-likelihood and non-linear least-squares algorithms to estimate the propagation distance along the RoF and the time-of-arrival between the RoF and the user equipment. For the case of linear PAs, we derive the Cramér-Rao lower bound to benchmark the performance of the estimators. Finally, we investigate the use of the system for uplink positioning. Our simulation results demonstrate that the proposed estimators perform satisfactorily even with the cascaded effects of non-linear PAs, and that the deployment of this RoF structure can enable new cost-effective opportunities for high-resolution positioning in indoor scenarios. In the numerical evaluation, we also use measured PMF characteristics for high-density polyethylene fibers.

**Index Terms**—Non-linear power amplifiers, polymer microwave fiber, radio over fiber, high-resolution positioning

## I. INTRODUCTION

Next-generation wireless communication systems are expected to support ubiquitous wireless connectivity. To achieve this goal, one crucial limitation is the spectrum resources. Therefore, the opportunities to use the abundance of the spectrum at the sub-terahertz (sub-THz) frequency band have been identified as a promising enabler for both ultra-high speed communications [2], [3] and high-resolution positioning [4]. This is largely so because sub-THz wireless systems can make use of a large bandwidth, allowing high data rates (up to several terabits per second) and high spatial resolution.

Although there has been abundant research on the performance of sub-THz wireless communication systems [5]–[7], their implementation is still challenging [8]. Considering the cost of sub-THz radio hardware and the limited

Dexin Kong, Diana Pamela Moya Osorio, and Erik G. Larsson are with Dept. of Electrical Engineering (ISY), Linköping University, 581 83 Linköping, Sweden (email: dexin.kong@liu.se; diana.moya.osorio@liu.se; erik.g.larsson@liu.se).

This work is an extended version of our conference paper presented at IEEE SPAWC 2024 [1]. This work was supported in part by ELLIT, and in part by the 6G Tandem project funded by the European Union's Horizon Europe research and innovation programme under Grant Agreement No 101096302.

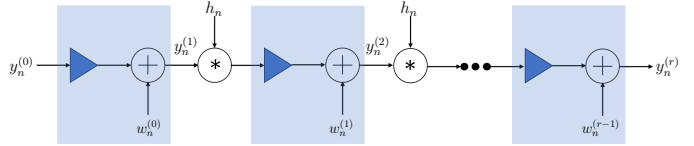


Fig. 1: Signal model for the RoF system with PAs and PMFs connected in cascade.

coverage [9], a low-cost and densely deployable solution is desirable. Recent developments in polymer microwave fiber (PMF) have motivated the development of radio-over-fiber (RoF) communications, which offers great opportunities for low-cost implementations of sub-THz wireless systems [10]–[12]. RoF systems can be implemented in different ways. Herein, we consider a system with a cascaded structure, where multiple radio units (RUs) are interconnected via low-cost PMFs and finally connected to a central unit (CU), where all signal processing is performed. Fig. 1 illustrates the cascade RoF system under consideration (the different variables will be introduced later). In this system, the signal propagates over a short-range sub-THz wireless channel and over multiple dispersive fibers within the RoF system. The salient feature of this system is that the propagation distance over the sub-THz wireless channel is only a small fraction of the distance between the CU and the user equipment (UE). Consequently, the overall propagation attenuation is significantly mitigated compared to that of a pure wireless sub-THz system of the same coverage. According to measurements reported in [13], PMFs attenuate sub-THz signals more than 2 dB per meter in the sub-THz spectrum. Hence, RUs have to be densely deployed to maintain the signal strength. RUs can either serve as access points or boosters (that amplify and forward the signals); thus the closest RU to the UE acts as access point and all other RUs between the entry/exit one and the CU act as boosters to compensate for the attenuation over the fiber. The RUs are equipped with antennas, a power amplifier (PA), and other radio frequency (RF) components. Since there are not digital signal processing units at the RUs, the cost of the system is significantly less than the dense deployment of radio transceivers.

For energy efficiency (EE) purposes, the PAs are allowed to operate in the non-linear regime [14]. Therefore, at each stage of the RoF system, the signals are distorted by a non-linear (PA) and a segment of dispersive PMF, with the latter being considered a linear time-invariant system. After multiple stages, the signal will be subjected to a cumulative distortion,

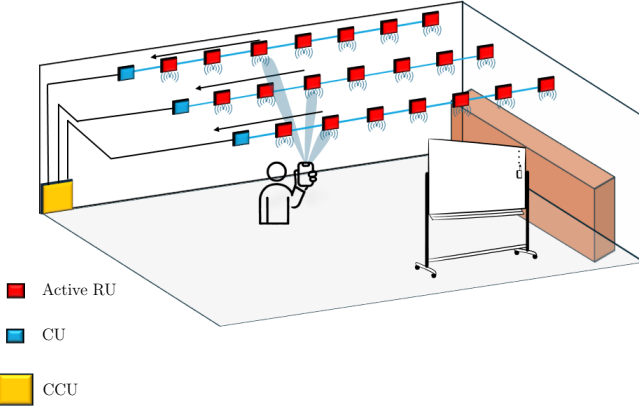


Fig. 2: An RoF system deployment in an indoor scenario.

which we exploit to estimate the propagation distance over the RoF. Thus, in combination with time-of-arrival (TOA) estimation over the wireless channel, the proposed system enables high-resolution positioning of UEs.

**Contributions:** The specific contributions of this paper are (i) an analysis of the cascaded structure with non-linear PAs and dispersive PMFs, and an analysis of the uplink (UL) signal; (ii) a maximum-likelihood (ML) framework and a non-linear least-squares (NLS) framework for the propagation distance estimation; (iii) a thorough evaluation on the performance of the estimators with PAs working in the linear regime via an analysis of Cramér-Rao lower bound (CRLB); (iv) numerical results (using measured PMF dispersion characteristics and different values of non-linear factors) demonstrate that the proposed estimators perform well on the propagation distance estimation even in the presence of the effects of cascaded non-linear PAs; and (v) we demonstrate the usability of the proposed system for high-resolution positioning in indoor scenarios. To the best of our knowledge, this is the first study of a RoF system with segments of dispersive PMFs and with non-linear amplifiers connected in cascade. The proposed system and analysis have the potential to open up several novel research directions and opportunities for positioning and localization systems.

The rest of this paper is organized as follows. Section II presents related works. Section III discusses the system overview and the structure of every component within a RoF. Section IV formulates the problem and the corresponding signal models. Section V evaluates the ML estimator in the linear regime by CRLB. Section VI shows the applied channel measurement data and numerical results. Section VII applies the proposed algorithm in an indoor positioning use case. Section VIII concludes the paper.

**Notations:** Boldface letters denote column vectors; regular letters denote scalars.  $(\cdot)^H$  denotes Hermitian transpose operation and  $(\cdot)^T$  denotes the transpose operation;  $\mathbb{C}$  is the set of complex numbers; The  $k$ th element of a column vector  $\mathbf{x}$  is denoted by the subscript as  $\mathbf{x}_k$ ; The superscript  $n$  of a vector/scalar  $(\cdot)^{(n)}$  denotes the vector/scalar at the  $n$ th RU of a RoF;  $|\cdot|$  denotes the absolute value;  $\|\cdot\|$  denotes the  $L^2$  norm;  $\delta(\cdot)$  is the delta function;  $\det(\cdot)$  calculates the determinant of

a matrix;  $\text{diag}\{\cdot\}$  represents a diagonal matrix;  $\mathbf{1}_N$  denotes a all one column vector with  $N$  elements; Finally,  $j = \sqrt{-1}$  is the imaginary unit.

## II. RELATED WORK

It is worth noting that this study considers a RoF system formed with only RF components and fibers. This implementation is novel and has not been investigated before, and it should not be confused with other RoF approaches that we introduce in the following.

Different from our proposal, a traditional RoF system considers the merging of radio frequency and optical fiber technologies, whose advantages are introduced in [15]. It is broadly acknowledged that RoF systems present low attenuation and high cost-efficiency due to the use of low-cost fibers whose development is reported in [10]–[12]. Moreover, since the signals in RoF systems are well confined within the fiber, these systems are not restricted in bandwidth. The work in [16] experimentally demonstrates the RoF systems in the THz frequency band, which implements a fiber-wireless seamless network in an indoor scenario. The reported results demonstrate good performance in terms of carrier-to-noise ratio. However, this type of RoF system often suffers from severe non-linearity in optical components, such as lasers [17], and materials [18], which represent the main challenge for RoF communications.

It is also worth differentiating the proposed system from radio stripes (RS), which is a commonly envisioned implementation of distributed massive MIMO (D-MMIMO). D-MMIMO distributes the antennas in a large area to provide ubiquitous service for every UE. The work in [19] provides a comprehensive overview of D-MMIMO in 6G. Although the D-MMIMO offers consistently high-quality service to all UEs, accurate synchronization between APs and the CU is challenging. On the other hand, RSs connect APs sequentially in one cable/fiber to the CU [20], which achieves simplified synchronization between APs via the shared bus. The authors in [21] investigate the high-accuracy positioning capability with RSs at the sub-6 GHz band. However, previous works about RS consider that every AP is equipped with full signal processing abilities, which are considerably expensive at THz frequencies. However, the unique structure considered in this paper allows dense and flexible deployment because the CU allocates all the resources and processes the signals. The studied system distinguishes itself from the distributed massive MIMO in the literature due to the absence of multiple antenna signal processing.

## III. SYSTEM OVERVIEW

Consider the system illustrated in Fig. 2, where multiple RoFs are deployed in parallel to serve UEs in an indoor scenario. Each RoF consists of  $U$  RUs and one CU at the end. One central coordination unit (CCU) connects the RoFs with the servers and coordinates different RoFs. All RUs are installed in the ceiling at the same height. The RUs are uniformly distributed, meaning the distance between two consecutive RUs in one RoF is fixed as  $\gamma$  and the distance

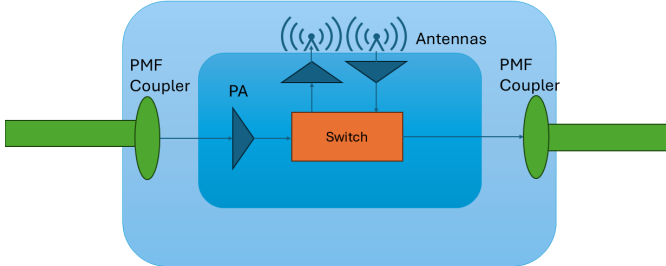


Fig. 3: Forward or receive configuration of the RU.

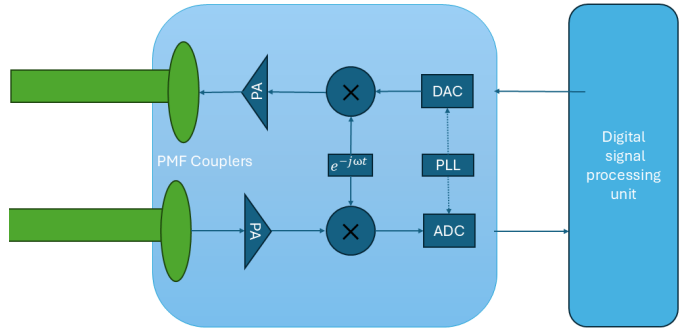


Fig. 5: Central unit.

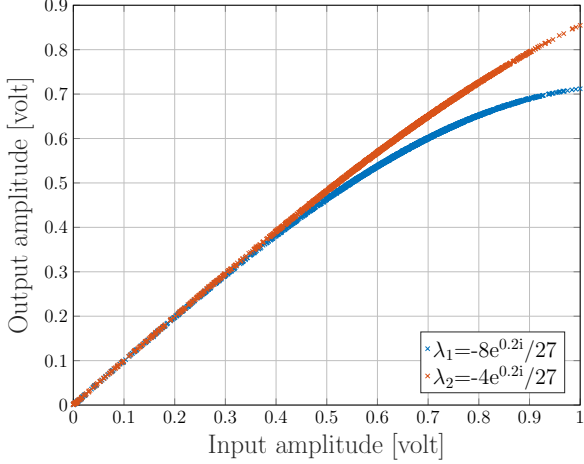


Fig. 4: Characteristics of the PA with different values of the non-linearity factor.

between any two RoFs is also fixed as  $\gamma$ . The location of the UE is denoted by  $(P_x, P_y, P_z)$  and the location of the  $r$ th RU in the  $m$ th RoF is denoted by  $(r\gamma, m\gamma, 0)$ . Therefore, the distance between the UE and the  $\text{RU}_{m,r}$  is calculated as

$$d_{m,r} = \sqrt{|P_x - r\gamma|^2 + |P_y - m\gamma|^2 + P_z^2}. \quad (1)$$

The configurations of RU, CU, and PMF will be discussed below. Other components are all considered to be linear filters having the same effect as the PMF.

#### A. Polymer microwave fiber

For a unit-length fiber segment, the channel impulse response with  $L$  taps and amplitudes  $([\beta_0, \beta_1, \dots, \beta_{L-1}]^T)$ <sup>1</sup> can be expressed as

$$h_n = \sum_{l=0}^{L-1} \beta_l \delta(n-l), \quad (2)$$

where  $n$  is the time index. Then, the impulse response of a fiber with  $r$  unit length can be expressed as

$$\tilde{h}_n = \underbrace{h_n * h_n * \dots * h_n}_{r \text{ convolutions}}, \quad (3)$$

<sup>1</sup>This model is valid in a non-linear system if the signals are oversampled properly.

where all factors in (3) are modeled as in (2). In the frequency domain, we consider the frequency response for a set of  $K$  discrete frequencies,  $\mathbf{f} = [f_0, \dots, f_{K-1}]^T$ . Thus, the frequency domain representation of (3) is given by the multiplication of frequency responses. Let  $\mathbf{H} = [H_0, \dots, H_{K-1}]^T$  represent the frequency response of a unit-length fiber. Then, the frequency response of a unit-length fiber at the  $k$ th frequency  $H_k$  is the Fourier transform of its impulse response given by

$$H_k = \sum_{n=0}^{N-1} h_n e^{-j2\pi f_k n T_s}, \quad (4)$$

where  $T_s$  is the sampling time interval. Hence, the frequency response of an  $r$ -units-long fiber, at the  $k$ th frequency, can be expressed as

$$\tilde{H}_k = \underbrace{H_k H_k \dots H_k}_{r \text{ multiplications}} = H_k^r. \quad (5)$$

#### B. Radio Unit

RUs are responsible for capturing incoming sub-THz signals, amplifying them, and forwarding them to the next component in the same stripe. Each RU consists of PMF couplers, PAs, antennas, and a switch as illustrated in Fig. 3. For the operation of the RoF system, we consider that each RU is equipped with a switch that selectively receives signals, either from the PMFs or the sub-THz antennas. When the RU detects signals from the PMFs, the switch disconnects the antenna input, allowing only the PMF signals to pass through. Thus, when the RU is configured to receive only PMF signals, it operated purely as a booster. Consequently, each UE is served exclusively by the nearest RU.

To understand the impact of non-linearities, we examine both regimes of operation of PAs, linear and non-linear.. The effects of non-linear PAs are characterized as a third-order polynomial with a factor  $\lambda$  [22], [23]. Therefore, relationship between the input  $x_n$  and output  $y_n$  of a PA is given by

- Linear regime:  $y_n = Gx_n$ ,
- Non-linear regime:  $y_n = G(x_n + \lambda x_n |x_n|^2)$ ,

where  $G$  is the amplification coefficient. Fig. 4 illustrates the characteristics of PA with different values of non-linear factors, where we can observe the non-linearity arises with a signal magnitude of  $\sim 0.4$  volts.

It should be noted that every RU is incapable of processing signals because of the absence of a digital signal

processing unit. From the perspective of expenditure, this design significantly lowers the price of each RU, since a digital processing unit is expensive in high frequencies. Conversely, this design disables the RU to mitigate signal impairments introduced by PAs and PMFs. As a consequence, this results in the accumulation of signal distortion along the propagation in a RoF system.

### C. Central unit

The CU is in charge of allocating resources, controlling the RUs, and processing data. Each CU comprises PAs, mixers, couplers, ADC/DAC, phase-locked loops (PLL), and a digital signal processing unit (see Fig. 5). The CU is capable to operate in full-duplex mode to communicate with one UE simultaneously.

## IV. PROBLEM FORMULATION AND SIGNAL MODEL

Consider the indoor scenario illustrated in Fig. 2, where the UE transmits data to multiple RoFs through the UL communication, where all RUs are active. Following the discussion in Section III, this paper considers two RU configurations with PAs working in both linear and non-linear regimes. In this paper, we assume all PAs have identical characteristics and work at the same operating point to simplify the analysis. Herein, the signals would experience the same distortion at every stage.

### A. RU with PAs operating in the linear regime

Under this scenario, the whole RS system is linear time-invariant. Thus, the signal model considers the dispersive channel of PMFs and the wireless channel from the UE to the entry RU. It is assumed that the UE transmits a known sequence of samples,  $s = [s_0, \dots, s_{K-1}]^T \in \mathbb{C}^{K \times 1}$  over  $K$  subcarriers. Initially, the signals undergo the wireless channel between the UE and the RU, which is unknown to the CU. Due to the sparse nature of the sub-THz wireless channel, the line-of-sight (LoS) components are considered to be dominant. Thus, the  $k$ th element of the input signal at the RoF,  $S_k$  with  $x = [x_0, x_1, \dots, x_{K-1}]^T$  (see Fig. 1), can be written as

$$x_k = Ae^{-j2\pi f_k \tau} s_k, \quad (6)$$

where

- $A$  is a complex value absorbing the effects of the wireless channel and the phase offset between the UE and the RoF. The magnitude of  $A$  represents the pathloss in LoS.
- $\tau$  is the unknown propagation delay including TOA and the clock offset, which can be expressed as

$$\tau = \frac{d}{c} + \delta_t \quad (7)$$

with  $c$  being the speed of light, and  $\delta_t$  being the clock offset between the UE and the RoF.

Note that distinguishing the effects of  $d$  and  $\delta_t$  is not possible since they have the same influence over the signals, i.e. phase shift and delay (see (7)). However, one can rely on the effects of cascaded fibers and PAs to estimate  $r$  and  $\tau$  separately.

The  $k$ th element of the output signal at the entry RU denoted as  $y_k^{(1)}$  is given by

$$y_k^{(1)} = GAe^{-j2\pi f_k \tau} s_k + w_k^{(0)}, \quad (8)$$

with  $w_k^{(r)} \sim \mathcal{CN}(0, \sigma^2)$  being the  $k$ th AWGN noise component at the  $r$ th RU. At the output of the next RU, after propagating through one segment of dispersive fiber and one PA, the signal at  $k$ th frequency is given by

$$y_k^{(2)} = G^2 H_k A e^{-j2\pi f_k \tau} s_k + GH_k w_k^{(0)} + w_k^{(1)}. \quad (9)$$

In a general form, after propagating through  $r$  RUs along the RoF, the received signal, with  $\mathbf{y} = [y_0, y_1, \dots, y_{K-1}]^T$ , at the CU can be written as

$$y_k^{(r)} = G^{(r+1)} H_k^r A e^{-j2\pi f_k \tau} s_k + \underbrace{G^{(r)} H_k^r w_k^{(0)} + \dots + w_k^{(r)}}_{(r+1) \text{ independent noises}}. \quad (10)$$

Note that the cumulative filtered noise by linear PAs and fibers still follow the Gaussian distribution since the linear transformation does not change the probability distribution. Let  $\tilde{w}_k$  denote the sum of independent Gaussian noise terms, then the variance of  $\tilde{w}_k$  is given by

$$\text{Var}(\tilde{w}_k) = \sum_{r'=0}^r b_k^{r'} \sigma^2. \quad (11)$$

where  $b_k \triangleq (G|H_k|)^2$ . Until now, parameter  $r$  takes discrete values, indicating the number of stages that the sub-THz signals propagate in a RoF. Since CRLB only applied to continuous-valued variables, we propose a continuous-value representation of  $r$  in Proposition 1.

**Proposition 1:** *The discrete-valued  $r$  in (10) can be approximated as a continuous value by splitting one RU into infinitely dense virtual RUs with length  $\Delta r \approx 0$ . The response of one virtual RU is  $(GH_k)^{\Delta r}$ . By accepting this approximation, the response of one RU is  $[(GH_k)^{\Delta r}]^{\frac{1}{\Delta r}}$ , which is equivalent to  $GH_k$ . The variance of effective noise at (11) can be rewritten as*

$$\text{Var}(\tilde{w}_k) = \sigma^2 \frac{\ln b_k}{b_k - 1} \int_0^{r+1} (b_k)^{r'} dr'. \quad (12)$$

*Proof:* the variance of  $\tilde{w}_k$  in (11) can be re-expressed as the sum of a geometric series as

$$\sum_{r'=0}^r b_k^{r'} \sigma^2 = \frac{1 - b_k^{r+1}}{1 - b_k} \sigma^2, \quad (13)$$

which is equal to the result of (12) as

$$\begin{aligned} \sigma^2 \frac{\ln b_k}{b_k - 1} \int_0^{r+1} (b_k)^{r'} dr' &= \frac{\ln b_k}{b_k - 1} \frac{b_k^{r+1} - 1}{\ln b_k} \sigma^2, \\ &= \frac{b_k^{r+1} - 1}{b_k - 1} \sigma^2. \end{aligned} \quad (14)$$

Note that (14) only holds for  $b_k \neq 1, \forall k$ . In other words, there are two cases worth being studied. Here, we name them as *flat fiber* and *frequency selective fiber* cases.

1) *Flat fiber*: Let us consider a special case in which the frequency response of the fiber is totally flat, that is the case for a system with very limited bandwidth. With the use of PMF,

the frequency response can be very flat at 1 GHz bandwidth. It is assumed that the amplification  $G$  is set to compensate for the attenuation, corresponding to  $b_k = 1, \forall k$ . Consequently, the variance of effective noise is

$$\Sigma = (r + 1)\sigma^2 \mathbf{I}_K, \quad (15)$$

and the phase shift induced by the fiber grows linearly with the propagation distance  $r$ . In other words, a flat fiber only supports one-mode transmission within the fiber, corresponding to a single-tap impulse response.

The unknown parameters to be estimated in this problem are  $\theta = [A, r, \tau]$ , of which the parameters  $r$  and  $\tau$  lead to a non-linear problem while  $A$  is involved linearly. We employ a maximum likelihood (ML) estimator to tackle this estimation problem. First, we define the vector  $\mathbf{g} \in \mathbb{C}^{K \times 1}$  as

$$\mathbf{g} = G^{r+1} [e^{-j2\pi f_0 \tau} H_0^r s_0, \dots, e^{-j2\pi f_{K-1} \tau} H_{K-1}^r s_{K-1}]^T. \quad (16)$$

The log-likelihood function can be written as

$$\ln P(\mathbf{y}^{(r)} | \theta) = \ln(\pi \det(\Sigma)) + (\mathbf{y}^{(r)} - A\mathbf{g})^H \Sigma^{-1} (\mathbf{y}^{(r)} - A\mathbf{g}). \quad (17)$$

Since  $A$  is linearly involved in the likelihood function and irrelevant to  $\Sigma$ , the estimation of  $A$  can be obtained as

$$\hat{A} = \min_A \|\mathbf{y}^{(r)} - A\mathbf{g}\|^2. \quad (18)$$

It is not difficult to obtain its estimate as

$$\hat{A} = \frac{\mathbf{g}^H \mathbf{y}^{(r)}}{\|\mathbf{g}\|^2}. \quad (19)$$

After dropping the dependency on  $A$  by utilizing  $\hat{A}$  and combining with the expression of  $\Sigma$  in (15), we can rewrite the objective function as

$$\begin{bmatrix} \hat{r} \\ \hat{\tau} \end{bmatrix} = \min_{r, \tau} \ln((r+1)K\pi\sigma^2) + \frac{\|\mathbf{y}^{(r)} - \mathbf{g}(\mathbf{g}^H \mathbf{g})^{-1} \mathbf{g}^H \mathbf{y}^{(r)}\|^2}{(r+1)\sigma^2}. \quad (20)$$

Therefore, after a two-dimensional grid search, the estimate  $\hat{r}$  as well as  $\hat{\tau}$ , can be obtained. The estimate of  $A$  is calculated as (19) by plugging in the estimates  $\hat{r}$  and  $\hat{\tau}$ .

2) *Frequency selective fiber*: A frequency selective fiber means the magnitude of its frequency response fluctuates over the bandwidth of interest, which makes  $b_k$  not equal to one. Without the loss of generality, we assume  $b_k \neq 1, \forall k$ , which ensures the validity of (14) for all frequencies. This is the case for a system with a large bandwidth, for example, 10 GHz. Consequently, the variance of effective noise is

$$\Sigma = \text{diag} \left\{ \frac{b_0^{r+1} - 1}{b_0 - 1} \sigma^2, \frac{b_1^{r+1} - 1}{b_1 - 1} \sigma^2, \dots, \frac{b_{K-1}^{r+1} - 1}{b_{K-1} - 1} \sigma^2 \right\}, \quad (21)$$

and the phase shifts introduced by the fiber might grow non-linearly with the propagation distance  $r$ . Similarly, one can view a *frequency selective fiber* to support multi-mode transmission, whose corresponding impulse response has multiple taps.

With the noise covariance being (21), prewhitening is applied by filtering the received signal  $\mathbf{y}^{(r)}$  and the vector  $\mathbf{g}$ ,

which can be written as

$$\begin{aligned} \tilde{\mathbf{y}}^{(r)} &= \Sigma^{-\frac{1}{2}} \mathbf{y}^{(r)}, \\ \tilde{\mathbf{g}} &= \Sigma^{-\frac{1}{2}} \mathbf{g}. \end{aligned} \quad (22)$$

Then, the estimate of  $A$  is obtained by (19), and the estimates of  $r$  and  $\tau$  are calculated as (20).

### B. RU with PAs operating in the non-linear regime

For EE purposes, the PAs are allowed to work in the non-linear regime, as modeled in Section III. As previously stated, the UE transmits a known sequence of samples  $\mathbf{s} = [s_0, \dots, s_{K-1}]^T$  over  $K$  subcarriers to the RoF. We model the input signal in the time domain as

$$x_n = \frac{1}{K} \sum_{k=0}^{K-1} e^{j2\pi \frac{n}{N} k} A e^{-j2\pi f_k \tau} s_k, \quad (23)$$

with  $x_n \in [x_0, x_1, \dots, x_{K-1}]^T$ .

The output of the entry RU can be written as

$$y_n^{(0)} = G \left( x_n + \underbrace{\lambda x_n |x_n|^2}_{\text{PA's non-linearity}} \right) + w_n^{(0)}. \quad (24)$$

To obtain the output at the following RUs, we define the function  $f(\cdot)$ , that combines the effects of a non-linear PA and one segment of PMF, and can be expressed as

$$f(y_n^{(0)}) = G \left( \sum_{l=0}^{L-1} \beta_l y_{n-l}^{(0)} + \lambda \sum_{l=1}^{L-1} \beta_l y_{n-l}^{(0)} \left| \sum_{l=1}^{L-1} \beta_l y_{n-l}^{(0)} \right|^2 \right). \quad (25)$$

If  $f(\cdot)$  in (25) takes a vector as input, it operates element-wise.

The signal  $\mathbf{y}^{(0)}$  would undergo  $r$  PAs and  $r$  segments of PMF to reach the CU. In other words, the signal  $\mathbf{y}^{(0)}$  would undergo a recursive process  $r$  times. Let  $f^r(\mathbf{y}^{(0)})$  be the overall function, which can be expressed as

$$f^r(\mathbf{y}^{(0)}) = \underbrace{f(f(f(\dots(\mathbf{y}^{(0)}))))}_{r \text{ times}}. \quad (26)$$

Therefore, the received signal at the CU can be expressed as  $\mathbf{y}^{(r)} = f^r(\mathbf{y}^{(0)}) + \mathbf{w}^{(r)}$ , where all the unknown parameters are interwoven with each other. As a result, we cannot apply the same estimator proposed in the linear regime ((19) and (20)). Alternatively, we can employ a NLS framework.

With PAs operating in the non-linear regime, a NLS framework may not serve as an optimal estimator as the noise distribution is transformed from a Gaussian distribution into another probability distribution. However, the output of a NLS framework will not deviate significantly from the optimum. Following the NLS framework, the objective function w.r.t. the unknown parameter  $A, r$ , and  $\tau$  is given by

$$\begin{bmatrix} \hat{A} \\ \hat{r} \\ \hat{\tau} \end{bmatrix} = \min_{A, \tau, r} \left\| \mathbf{y}^{(r)} - f^r \left( G \left( x_n + \lambda x_n |x_n|^2 \right) \right) \right\|^2, \quad (27)$$

where a three-dimensional grid search is needed to obtain the estimates. To solve this problem, we employ a particle swarm optimization (PSO) algorithm described in Algorithm 1, to

reduce the complexity compared to a three-dimensional grid search.

Compared to the ML estimator in (17), the employed NLS framework in the non-linear regime disregards the information contained in the noise covariance.

## V. CRAMÉR-RAO LOWER BOUND

CRLB is a very useful tool for evaluating the performance of any unbiased estimator, as it provides a measure of the lower limit of the variance. However, the CRLB for the case of PAs operating in the non-linear regime leads to a cumbersome problem due to the presence of iterative non-linearity in the signal model. Alternatively, this section introduces the CRLB of the proposed ML estimator with PAs operating in the linear regime as a benchmark of estimation accuracy.

For simplicity, we express the complex valued  $A$  and  $H$  with their magnitudes  $|A|$  and  $|H_k|$  and phases  $\phi$  and  $\psi_k$ , i.e.,  $A = |A|e^{j\phi}$  and  $H = |H_k|e^{j\psi_k}$ . Hence, the unknown parameters are defined as  $\boldsymbol{\theta} \triangleq [|A|, \phi, \tau, r]^T$ .

The definition for the CRLB is given by

$$[\text{Var}(\hat{\boldsymbol{\theta}}_i)] \geq [\mathbf{I}^{-1}(\boldsymbol{\theta})]_{i,i}, \quad (28)$$

where  $\mathbf{I}(\boldsymbol{\theta})$  is the Fisher information matrix (FIM) for the vector  $\boldsymbol{\theta}$  and is defined as

$$\begin{aligned} [\mathbf{I}(\boldsymbol{\theta})]_{i,j} &= \text{tr} \left\{ \mathbf{C}(\boldsymbol{\theta})^{-1} \frac{\partial \mathbf{C}(\boldsymbol{\theta})}{\partial \theta_i} \mathbf{C}(\boldsymbol{\theta})^{-1} \frac{\partial \mathbf{C}(\boldsymbol{\theta})}{\partial \theta_j} \right\} \\ &+ 2\Re \left\{ \frac{\partial \boldsymbol{\mu}(\boldsymbol{\theta})^H}{\partial \theta_i} \mathbf{C}(\boldsymbol{\theta})^{-1} \frac{\partial \boldsymbol{\mu}(\boldsymbol{\theta})}{\partial \theta_j} \right\}, \end{aligned} \quad (29)$$

which reveals the amount of information associated with each pair of unknown parameters. One important characteristic of FIM is that every FIM is positive semi-definite, indicating the information content is non-negative and ensuring its eigenvalues are non-negative. Moreover, a positive definite FIM indicates the parameters are identifiable and a singular FIM indicates the parameters are non-identifiable.

As mentioned in Section IV, there are two expressions for the variance of effective noise as shown in (15) and in (21). Naturally, the CRLB needs to be calculated for both flat fiber and frequency selective fiber cases. Detailed calculations can be found in the Appendix A.

### A. CRLB for flat fiber

Now, let us start with the flat fiber case, whose  $\mathbf{C}(\boldsymbol{\theta})$  and  $\boldsymbol{\mu}(\boldsymbol{\theta})$  are defined as

$$\begin{aligned} \mathbf{C}(\boldsymbol{\theta}) &= (r+1)\sigma^2 \mathbf{I}_K \\ \boldsymbol{\mu}(\boldsymbol{\theta}) &= \left[ G^{r+1} |A| |H_0|^r s_0 e^{j(\phi+r\psi_0-2\pi f_0 \tau)}, \dots, \right. \\ &\quad \left. G^{r+1} |A| |H_{K-1}|^r s_{K-1} e^{j(\phi+r\psi_{K-1}-2\pi f_{K-1} \tau)} \right]^T. \end{aligned} \quad (30)$$

Therefore, partial derivatives in (29) can be calculated as

$$\left[ \frac{\partial \boldsymbol{\mu}(\boldsymbol{\theta})}{\partial |A|} \right]_k = G e^{j(\phi+r\psi_k-2\pi f_k \tau)} s_k, \quad (31a)$$

$$\left[ \frac{\partial \boldsymbol{\mu}(\boldsymbol{\theta})}{\partial \phi} \right]_k = jG |A| s_k e^{j(\phi+r\psi_k-2\pi f_k \tau)}, \quad (31b)$$

$$\left[ \frac{\partial \boldsymbol{\mu}(\boldsymbol{\theta})}{\partial \tau} \right]_k = -j2\pi f_k G |A| s_k e^{j(\phi+r\psi_k-2\pi f_k \tau)}, \quad (31c)$$

$$\left[ \frac{\partial \boldsymbol{\mu}(\boldsymbol{\theta})}{\partial r} \right]_k = G |A| e^{j(\phi+r\psi_k-2\pi f_k \tau)} s_k (j\psi_k). \quad (31d)$$

According to the symmetry property,  $[\mathbf{I}(\boldsymbol{\theta})]_{i,j} = [\mathbf{I}(\boldsymbol{\theta})]_{j,i}$  is always valid so that there are 10 unique entries in each FIM. Regarding the *flat fiber*, the elements of the FIM are calculated as

$$[\mathbf{I}(\boldsymbol{\theta})]_{|A|,|A|} = 2 \frac{G^2}{(r+1)\sigma^2} \sum_{k=0}^{K-1} |s_k|^2, \quad (32a)$$

$$[\mathbf{I}(\boldsymbol{\theta})]_{|A|,\phi} = 0, \quad (32b)$$

$$[\mathbf{I}(\boldsymbol{\theta})]_{|A|,\tau} = 0, \quad (32c)$$

$$[\mathbf{I}(\boldsymbol{\theta})]_{|A|,r} = 0, \quad (32d)$$

$$[\mathbf{I}(\boldsymbol{\theta})]_{\phi,\phi} = 2 \frac{G^2 |A|^2}{(r+1)\sigma^2} \sum_{k=0}^{K-1} |s_k|^2, \quad (32e)$$

$$[\mathbf{I}(\boldsymbol{\theta})]_{\phi,\tau} = -\frac{4\pi G^2 |A|^2}{(r+1)\sigma^2} \sum_{k=0}^{K-1} f_k |s_k|^2, \quad (32f)$$

$$[\mathbf{I}(\boldsymbol{\theta})]_{\phi,r} = 2 \frac{G^2 |A|^2}{(r+1)\sigma^2} \sum_{k=0}^{K-1} |s_k|^2 \psi_k, \quad (32g)$$

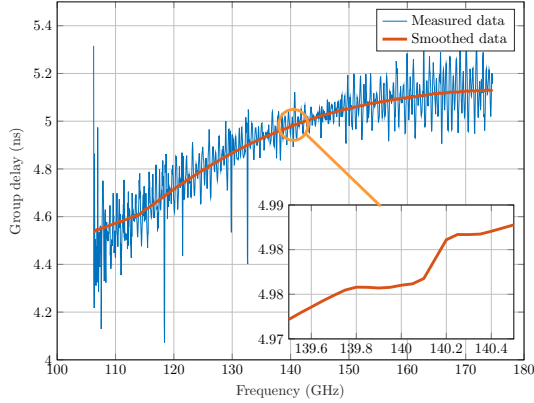
$$[\mathbf{I}(\boldsymbol{\theta})]_{\tau,\tau} = \frac{8\pi^2 G^2 |A|^2}{(r+1)\sigma^2} \sum_{k=0}^{K-1} f_k^2 |s_k|^2, \quad (32h)$$

$$[\mathbf{I}(\boldsymbol{\theta})]_{r,r} = \frac{K}{(r+1)^2} + 2 \frac{G^2 |A|^2}{(r+1)\sigma^2} \sum_{k=0}^{K-1} |s_k|^2 \psi_k^2, \quad (32i)$$

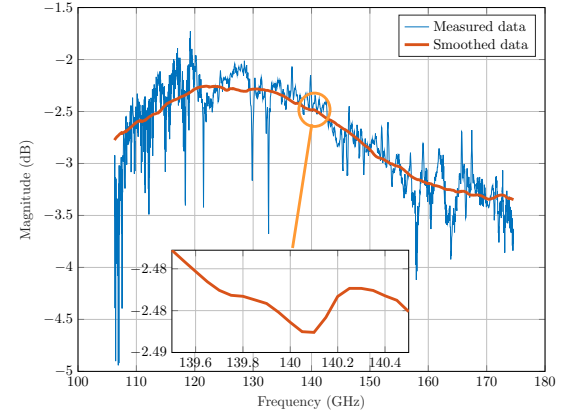
$$[\mathbf{I}(\boldsymbol{\theta})]_{\tau,r} = -\frac{4\pi G^2 |A|^2}{(r+1)\sigma^2} \sum_{k=0}^{K-1} |s_k|^2 f_k \psi_k. \quad (32j)$$

**Discussions:** The main takeaways from the CRLB calculation, from (32a) to (32j), are:

- The estimate of  $|A|$  is solely dependent on the received signal-to-noise ratio (see (32a)).
- As shown in (32f), (32g), and (32j), there is a coupling between the estimates of  $\tau$ ,  $r$ , and  $\phi$ , which is proved to make the FIM close to a singular matrix through numerical results in the following section.
- The phase shifts introduced by the fiber are interwoven with the phase shifts introduced from the wireless channel and the phase offset, making it impossible for the system to identify the propagation distance  $r$  based on the phase information.
- According to (32i), the system can rely on the overall noise variance to estimate the propagation distance, as it accumulates linearly with  $r$ .



(a) Group delay



(b) Magnitude

Fig. 6: Measured characteristics of a 1-meter PMF made of high-density polyethylene with a solid rectangular cross-section in the D-band (110 GHz to 170 GHz) [13]: (a) Group delay; (b) Magnitude.

### B. CRLB for frequency selective fiber

For the frequency selective fiber case, the noise variance is defined as

$$\begin{aligned} \mathbf{C}(\boldsymbol{\theta}) &= \text{diag} \left( \sigma^2 \frac{\ln b_0}{b_0 - 1} \int_0^{r+1} (b_0)^{r'} dr', \dots, \right. \\ &\quad \left. \sigma^2 \frac{\ln b_{K-1}}{b_{K-1} - 1} \int_0^{r+1} (b_{K-1})^{r'} dr' \right), \\ [\mathbf{C}^{-1}(\boldsymbol{\theta})]_{k,k} &= \frac{b_k - 1}{\sigma^2(b_k^{r+1} - 1)}, \\ \left[ \frac{\partial \mathbf{C}(\boldsymbol{\theta})}{\partial r} \right]_{k,k} &= \frac{\sigma^2 b_k^{r+1} \ln b_k}{b_k - 1}, \end{aligned} \quad (33)$$

and  $\boldsymbol{\mu}(\boldsymbol{\theta})$  is the same as (30). One can derive the first-order derivatives as

$$\left[ \frac{\partial \boldsymbol{\mu}(\boldsymbol{\theta})}{\partial |A|} \right]_k = G^{(r+1)} |H_k|^r e^{j(\phi + r\psi_k - 2\pi f_k \tau)} s_k, \quad (34a)$$

$$\left[ \frac{\partial \boldsymbol{\mu}(\boldsymbol{\theta})}{\partial \phi} \right]_k = j G^{(r+1)} |A| |H_k|^r s_k e^{j(\phi + r\psi_k - 2\pi f_k \tau)}, \quad (34b)$$

$$\left[ \frac{\partial \boldsymbol{\mu}(\boldsymbol{\theta})}{\partial \tau} \right]_k = -j 2\pi f_k G^{(r+1)} |A| |H_k|^r s_k e^{j(\phi + r\psi_k - 2\pi f_k \tau)}, \quad (34c)$$

$$\begin{aligned} \left[ \frac{\partial \boldsymbol{\mu}(\boldsymbol{\theta})}{\partial r} \right]_k &= G^{(r+1)} |A| |H_k|^r s_k e^{j(\phi + r\psi_k - 2\pi f_k \tau)} \\ &\quad \times (\ln \sqrt{b_k} + j\psi_k). \end{aligned} \quad (34d)$$

Similarly, the entries in the FIM can be obtained as

$$[\mathbf{I}(\boldsymbol{\theta})]_{|A|,|A|} = 2G^2 \sum_{k=0}^{K-1} \frac{(b_k - 1)b_k^r |s_k|^2}{\sigma^2(b_k^{r+1} - 1)}, \quad (35a)$$

$$[\mathbf{I}(\boldsymbol{\theta})]_{|A|,\phi} = 0, \quad (35b)$$

$$[\mathbf{I}(\boldsymbol{\theta})]_{|A|,\tau} = 0, \quad (35c)$$

$$[\mathbf{I}(\boldsymbol{\theta})]_{|A|,r} = 2G^2 |A| \sum_{k=0}^{K-1} \frac{(b_k - 1)b_k^r |s_k|^2 \ln \sqrt{b_k}}{\sigma^2(b_k^{r+1} - 1)}, \quad (35d)$$

$$[\mathbf{I}(\boldsymbol{\theta})]_{\phi,\phi} = 2G^2 |A|^2 \sum_{k=0}^{K-1} \frac{(b_k - 1)b_k^r |s_k|^2}{\sigma^2(b_k^{r+1} - 1)}, \quad (35e)$$

$$[\mathbf{I}(\boldsymbol{\theta})]_{\phi,\tau} = -4\pi G^2 |A|^2 \sum_{k=0}^{K-1} \frac{(b_k - 1)f_k b_k^r |s_k|^2}{\sigma^2(b_k^{r+1} - 1)}, \quad (35f)$$

$$[\mathbf{I}(\boldsymbol{\theta})]_{\phi,r} = 2G^2 |A|^2 \sum_{k=0}^{K-1} \frac{(b_k - 1)b_k^r |s_k|^2 \psi_k}{\sigma^2(b_k^{r+1} - 1)}, \quad (35g)$$

$$[\mathbf{I}(\boldsymbol{\theta})]_{\tau,\tau} = 8\pi^2 G^2 |A|^2 \sum_{k=0}^{K-1} \frac{(b_k - 1)f_k^2 b_k^r |s_k|^2}{\sigma^2(b_k^{r+1} - 1)}, \quad (35h)$$

$$[\mathbf{I}(\boldsymbol{\theta})]_{\tau,r} = -4\pi G^2 |A|^2 \sum_{k=0}^{K-1} \frac{(b_k - 1)b_k^r |s_k|^2 f_k \psi_k}{\sigma^2(b_k^{r+1} - 1)}, \quad (35i)$$

$$\begin{aligned} [\mathbf{I}(\boldsymbol{\theta})]_{r,r} &= 2G^2 |A|^2 \sum_{k=0}^{K-1} \frac{|s_k|^2 (b_k - 1)b_k^r ((\ln \sqrt{b_k})^2 + \psi_k^2)}{\sigma^2(b_k^{r+1} - 1)} \\ &\quad + \sum_{k=0}^{K-1} \left( \frac{b_k^r \ln b_k}{1 - b_k^{r+1}} \right)^2. \end{aligned} \quad (35j)$$

**Discussion:** Based on the CRLB obtained for the frequency selective fiber, one can observe

- With the use of frequency selective fiber, a coupling between  $|A|$  and  $r$  appears as illustrated in (35d), which comes from the varied magnitude of the frequency response of the PMF.
- As illustrated in (35j), the system can rely on the shape of the spectrum of the received signal at CU, while it can only rely on the noise variance with a flat fiber (see (32i)).
- The coupling between  $\phi$ ,  $\tau$ , and  $r$  still exists (see (35g), (35f), and (35i)).

## VI. SIMULATION RESULTS

In this section, we first validate the proposed NLS estimator, relying on the measured channel of a segment of PMF. Then,

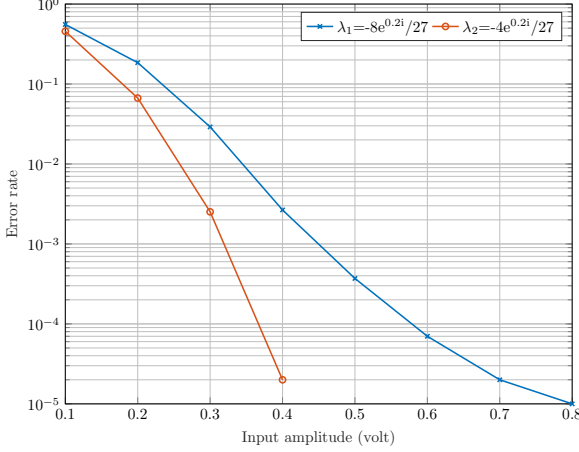


Fig. 7: The error rate of  $\hat{r} \neq r$ .

we validate the proposed CRLB with two artificial channels generated under a constraint in the total energy.

#### A. Validation of the proposed estimators with measured fiber channel characteristics

In this section, we illustrate the performance obtained by the proposed estimators with the fiber channel measurements presented in [13]. These measurements inherently include several imperfections, such as noise, interference, and measurement errors. Therefore, a median filtering with a window size of 300 is implemented through Matlab to smooth the data in group delay and magnitude, separately. Both the smoothed data and the original data are shown in Figs. 6a and 6b. The measured data consists of channel characteristics at  $K$  discrete frequencies, encompassing both magnitudes ( $|\mathbf{H}| = [|H_0|, \dots, |H_{K-1}|]^T$ ) and group delay. Subsequently, the phase response  $\psi = [\psi_0, \dots, \psi_{K-1}]^T$  was obtained by integrating the group delay on the discrete frequencies. Then, the transfer function can be expressed as

$$\mathbf{H} = |\mathbf{H}| \circ \exp(j\psi), \quad (36)$$

where  $\circ$  represents the Hadamard product. The employed LOS pathloss model comprises free-space path loss and a large-scale fading component, which can be written as

$$|A| = G_t G_r \left( \frac{\lambda}{2\pi d} \right)^2 + \zeta, \quad (37)$$

with  $\lambda$  being the wavelength,  $d$  being defined in (1),  $G_t$  and  $G_r$  being the transmitter gain, and receiver gain respectively. The large-scale fading component  $\zeta$  follows a log-normal distribution with a standard deviation of 2 dB. This model can be replaced by other developed LoS models for sub-THz propagation, such as the 3GPP model in [24].

Monte Carlo simulations were performed with a RoF system comprising five RUs and one CU. Between every two components, a fiber with the frequency response as expressed in (36) serves as the connection. Distortion incurred by PAs was illustrated in Fig. 4. The UE transmits a known sequence of

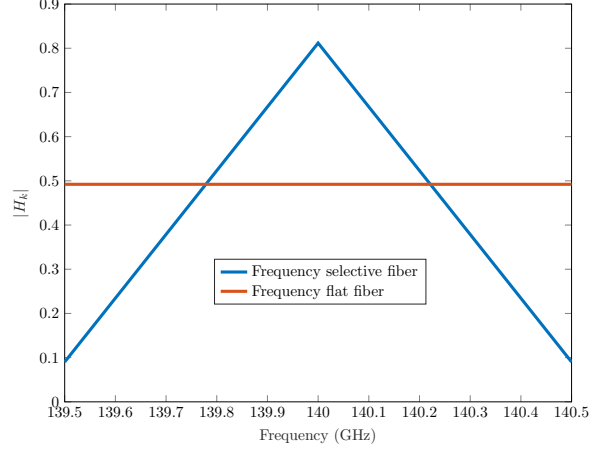


Fig. 8: The magnitude of the frequency response for the frequency-flat fiber and the frequency-selective fiber.

samples using a quadrature phase shift keying waveform with a unit amplitude. The UE accesses the RoF system through the third RU. The channel magnitude illustrated in Fig. 6b corresponds to a spectrum with 1 GHz bandwidth centered around 140 GHz, from which the maximum magnitude in a one-meter fiber is approximately -2.48 dB. Therefore,  $G$  is set to 2.48 dB for PAs. The parameters in (37) were set to ensure the input amplitude is in a certain regime (linear or non-linear) of the PAs.

The proposed PSO was implemented in Matlab and the results are shown in Fig. 7. It is observed that the error rate would decrease to a level of  $10^{-5}$  with a proper input amplitude, which indicates that the proposed algorithm is able to accurately estimate the propagation distance even when PAs work in the non-linear regime. Through comparison between the estimation accuracy with two non-linear factors, one can observe an accuracy loss with a higher non-linear factor.

#### B. Validation of CRLB with assumed fiber channels

To validate the CRLB calculated, extensive Monte-Carlo simulations were performed and based on two artificial channels shown in Fig. 8, corresponding to a flat fiber (red curve) and a frequency selective fiber (blue curve). Each channel contains the same amount of energy, i.e.,  $\sum_{k=0}^{K-1} |H_k|^2 = \mathcal{E}$ . It should be emphasized that the shape of the spectrum of a frequency selective fiber does not impose any deviation in the conclusions of this paper. The corresponding root mean squared error (RMSE) of target parameters was calculated and plotted in Figs. 9, and 10.

The comparison between the CRLB w.r.t.  $\hat{r}$  with a flat fiber and that with a non-flat fiber indicates the estimation accuracy is enhanced with a frequency selective fiber, which proves the fact that the system can extract additional information from the spectrum of the received signal. Another observation from Fig. 9 is a flat bound with a flat fiber. This understanding can be acquired from (32i), where the CU estimates the noise variance and determines its quantitative relationship with

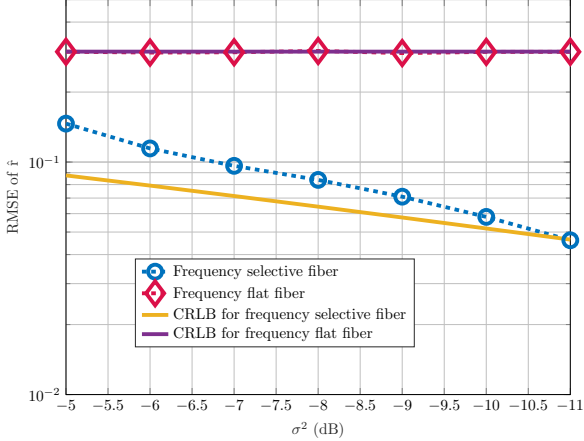


Fig. 9: RMSE and CRLB of  $\hat{r}$ , with frequency flat and frequency selective fibers.

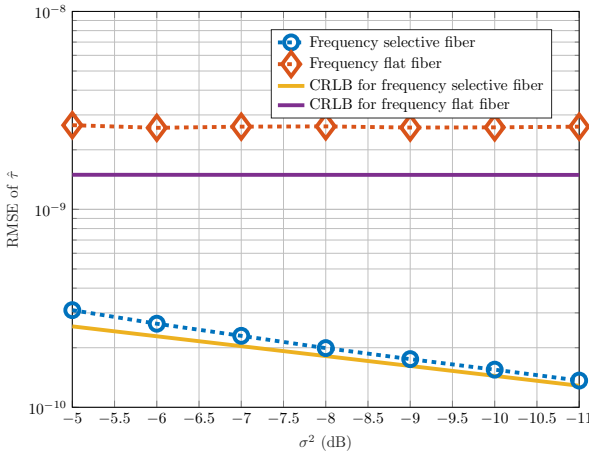


Fig. 10: RMSE and CRLB of  $\hat{\tau}$ , with frequency flat and frequency selective fibers.

the noise variance  $\sigma^2$  at each PA. Therefore, this bound is independent of the exact value of  $\sigma^2$ . The ML estimator achieves an RMSE equal to the CRLB, indicating that it attains optimal performance. Similar conclusions can be drawn from Fig 10. It is worth noting that the gap between the RMSE of certain estimates and the corresponding CRLB does not necessarily indicate suboptimality, as the simulation grids are inherently constrained.

## VII. USE CASE: INDOOR POSITIONING

A pertinent use case for the proposed estimation framework on the considered RoF system is indoor positioning. This low-cost design allows the operator to densely deploy RoFs for extreme data rate and good coverage. Here, we assume a UE moves along a trajectory in an indoor scenario illustrated in Fig. 2, where three RoFs are serving the UE simultaneously. The UE is assumed to have an isotropic antenna, while each RU is equipped with a phased array. To ensure fairness and avoid potential biases, no additional assumptions about the

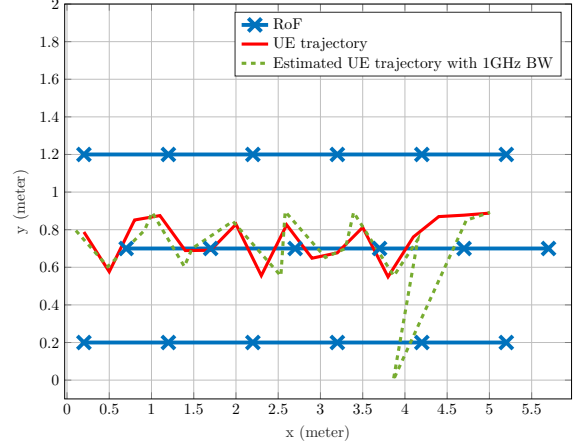


Fig. 11: Floorplan of an indoor scenario with three RoFs, a UE trajectory, and the estimated UE trajectory with 1GHz bandwidth.

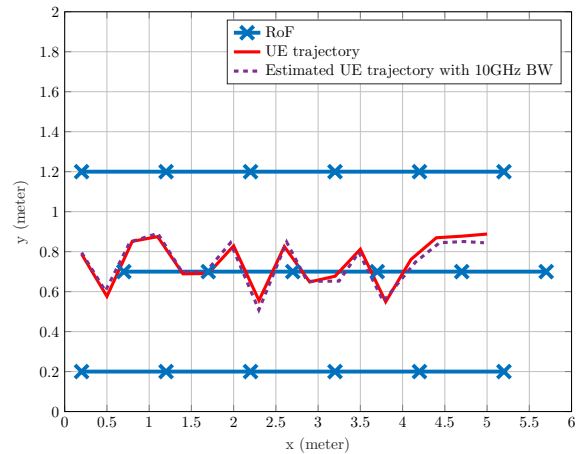


Fig. 12: Floorplan of an indoor scenario with three RoFs, a UE trajectory, and the estimated UE trajectory with 10GHz bandwidth.

antennas are made. Instead, it is simply assumed that the UE is consistently served by three RUs located at three RoFs.

The height of the UE is assumed to be consistently 1.5 meters below the ceiling at all positions, with a uniform spacing of 1 meter between different RUs and between different RoFs. According to (1), the distance between the UE and the entry RU is written as

$$d_{m,r} = \sqrt{(P_x - r)^2 + (P_y - m)^2 + 1.5^2}. \quad (38)$$

Let the vector  $\mathbf{d} \triangleq [d_{1,r_1}, d_{2,r_2}, d_{3,r_3}]^T$  store the distances between the UE and three entry RUs. The time-of-flight from the UE to the entry RU is interwoven with a clock offset as defined in (7), which can be viewed as a bias. The position of the UE  $P_x, P_y$  is estimated through the estimated  $\tau =$

$(1/c)\mathbf{d} + \mathbf{1}_3\delta_t$  at three RoFs and can be written as

$$\begin{bmatrix} \hat{P}_x \\ \hat{P}_y \end{bmatrix} = \min_{P_x, P_y, \delta_t} \left\| \boldsymbol{\tau} - \frac{\mathbf{d}}{c} - \mathbf{1}_3\delta_t \right\|^2, \quad (39)$$

where the estimation of  $\delta_t$  is a linear model with the rest of quantities. Let  $\mathbf{R} \triangleq \boldsymbol{\tau} - \frac{\mathbf{d}}{c}$ . It is not difficult to write the estimate of  $\delta_t$  as

$$\hat{\delta}_t = \frac{\mathbf{1}_3^T \mathbf{R}}{\mathbf{1}_3^T \mathbf{1}_3}. \quad (40)$$

Plugging in  $\hat{\delta}_t$  back to (39), the estimate of the UE positions can be written as

$$\begin{bmatrix} \hat{P}_x \\ \hat{P}_y \end{bmatrix} = \min_{P_x, P_y} \left\| \mathbf{R} - \mathbf{1}_3(\mathbf{1}_3^T \mathbf{1}_3)^{-1} \mathbf{1}_3^T \mathbf{R} \right\|^2. \quad (41)$$

Simulations were conducted using bandwidths of 1 GHz and 10 GHz, corresponding to delay resolutions of 0.3 meters and 0.03 meters, respectively. Figs. 11 and 12 show the estimated UE trajectories with different bandwidths. The RMSE of the estimated positions, obtained through Monte Carlo simulations, is 0.04 meters for 10 GHz and 0.5 meters for 1 GHz, both closely approaching their respective delay resolutions.

## VIII. CONCLUSION

This paper studied a novel, low-cost, and easily deployable sub-THz RoF system implementation that combines PMFs and RUs in a cascaded structure. An UL signal model of this system was developed by considering two regimes for PAs, linear and non-linear. For our analysis, we considered two type of fibers: flat fibers and frequency selective fibers, whose effects were included in the signal model. Based on this model, an ML framework and a NLS framework were developed to estimate the propagation distance along the RoF and the TOA of signals transmitted from a UE. The CRLB was derived as a benchmark of the variance of the proposed ML estimator.

Monte-Carlo simulations were performed to assess the performance of the proposed estimator. Our results demonstrate that good performance of the proposed estimators can be achieved under the effects of cascaded PMFs and RUs. The ML estimator achieves superior performance for a frequency-selective fiber compared to with a frequency-flat fiber. Finally, our proposed algorithms show high accuracy in positioning UEs in an indoor scenario.

A future direction could be estimating how the second moment of the variance is affected by the non-linearities and including that into the estimation criterion. Another possible direction is to replace the third-order polynomial model of PA non-linearity with a more accurate one.

## ACKNOWLEDGMENT

We thank Dr. Frida Strömbeck and Prof. Herbert Zirath from Chalmers University of Technology for generously sharing the measured PMF characteristics that we used in our numerical examples.

## Algorithm 1: Particle Swarm Optimization Algorithm

```

1 Function Cost( $\theta, \lambda, G, s, f(x), \mathbf{y}^{(r)}$ ):
2   (23);
3   (25);
4    $c \leftarrow (27)$ ;
5   return  $c$ ;
6 Function PSO( $\lambda, G, H, s, \mathbf{y}^{(r)}, f(x)$ ):
7    $m \leftarrow 100$ ; // Set the #iterations
8    $p \leftarrow 1000$ ; // Set particle size
9    $w_1 \leftarrow 1$ ; // personal best pos. Weights
10   $w_2 \leftarrow 0.7$ ; // global best pos. Weights
11   $w_{\text{ine}} \leftarrow 0.3$ ; // Set inertia weight
12   $n \leftarrow 4$ ; // #variables
13   $c_{\text{gbest}} \leftarrow 0$   $v \leftarrow 0$ ;
14   $\theta_{\text{min}} \leftarrow [|A|_{\text{min}}, \phi_{\text{min}}, \tau_{\text{min}}, r_{\text{min}}]$ ;
15   $\theta_{\text{max}} \leftarrow [|A|_{\text{max}}, \phi_{\text{max}}, \tau_{\text{max}}, r_{\text{max}}]$ ;
16  for  $i \leftarrow 1$  to  $p$  do
17    for  $j \leftarrow 1$  to  $n$  do
18       $\theta(i, j) \leftarrow (\theta_{\text{max}}(j) - \theta_{\text{min}}(j)) * \text{rand}(1) + \theta_{\text{min}}(j)$ ;
19       $\theta_{\text{aux}}(j) \leftarrow \theta(i, j)$ ;
20     $c(i) \leftarrow \text{Cost}(\theta_{\text{aux}}, \lambda, G, s, f(x), \mathbf{y}^{(r)})$ ;
21    if  $c(i) < c_{\text{gbest}}$  then
22       $c_{\text{gbest}} \leftarrow c(i)$ ;
23      for  $j \leftarrow 1$  to  $n$  do
24         $\theta_{\text{gbest}}(j) \leftarrow \theta(i, j)$ ;
25   $\theta_{\text{pbest}} \leftarrow \theta$ ,  $c_{\text{pbest}} \leftarrow c$ ;
26  for  $i \leftarrow 1$  to  $m$  do
27     $v \leftarrow w_{\text{ine}} * v + w_1 * \text{rand}(p, n) * (\theta_{\text{pbest}} - \theta) + w_2 * \text{rand}(p, n) * (\theta_{\text{gbest}} - \theta)$ ;
28     $\theta \leftarrow \theta + v$ ;
29    for  $j \leftarrow 1$  to  $p$  do
30      for  $k \leftarrow 1$  to  $n$  do
31        if  $\theta(j, k) < \theta_{\text{min}}(k)$  then
32           $\theta(j, k) \leftarrow \theta_{\text{min}}(k)$ ;
33        if  $\theta(j, k) > \theta_{\text{max}}(k)$  then
34           $\theta(j, k) \leftarrow \theta_{\text{max}}(k)$ ;
35         $\theta_{\text{aux}}(k) \leftarrow \theta(j, k)$ ;
36       $c(j) \leftarrow \text{Cost}(\theta_{\text{aux}}, \lambda, G, s, f(x), \mathbf{y}^{(r)})$ ;
37      if  $c(j) < c_{\text{pbest}}(j)$  then
38         $c_{\text{pbest}}(j) \leftarrow c(j)$ ;
39        for  $k \leftarrow 1$  to  $n$  do
40           $\theta_{\text{pbest}}(j, k) \leftarrow \theta(j, k)$ ;
41      if  $c(j) < c_{\text{gbest}}$  then
42         $c_{\text{gbest}} \leftarrow c(j)$ ;
43        for  $k \leftarrow 1$  to  $n$  do
44           $\theta_{\text{gbest}}(k) \leftarrow \theta(j, k)$ ;
45   $w_{\text{ine}} \leftarrow w_{\text{ine}} * 0.7$ ;
46  return  $c_{\text{gbest}}, \theta_{\text{gbest}}$ ;

```

## REFERENCES

[1] D. Kong, D. P. Moya Osorio, and E. G. Larsson, "Propagation distance estimation for radio over fiber with cascaded structure," in *Proc. of 2024*

*IEEE 25th International Workshop on Signal Processing Advances in Wireless Communications (SPAWC)*, 2024, pp. 691–695.

[2] Z. Chen, X. Ma, B. Zhang, Y. Zhang, Z. Niu, N. Kuang, W. Chen, L. Li, and S. Li, “A survey on Terahertz communications,” *China Communications*, vol. 16, no. 2, pp. 1–35, 2019.

[3] X. Cai, X. Cheng, and F. Tufvesson, “Toward 6G with Terahertz communications: Understanding the propagation channels,” *IEEE Communications Magazine*, vol. 62, no. 2, pp. 32–38, 2024.

[4] A. Bourdoux, A. N. Barreto, B. van Liempd, C. de Lima, D. Dardari, D. Belot, E.-S. Lohan, G. Seco-Granados, H. Sarieddeen, H. Wymeersch *et al.*, “6G white paper on localization and sensing,” *arXiv preprint arXiv:2006.01779*, 2020.

[5] H. Elayan, O. Amin, R. M. Shubair, and M.-S. Alouini, “Terahertz communication: The opportunities of wireless technology beyond 5G,” in *Proc. of 2018 International Conference on Advanced Communication Technologies and Networking (CommNet)*, 2018, pp. 1–5.

[6] C. Chaccour, W. Saad, O. Semiai, M. Bennis, and P. Popovski, “Joint sensing and communication for situational awareness in wireless THz systems,” in *Proc. of IEEE International Conference on Communications (ICC)*, 2022, pp. 3772–3777.

[7] O. Kanhere and T. S. Rappaport, “Outdoor sub-THz position location and tracking using field measurements at 142 GHz,” in *Proc. of IEEE International Conference on Communications (ICC)*, 2021, pp. 1–6.

[8] P. Heydari, “Terahertz integrated circuits and systems for high-speed wireless communications: Challenges and design perspectives,” *IEEE Open Journal of the Solid-State Circuits Society*, vol. 1, pp. 18–36, 2021.

[9] E. Björnson, L. Van der Perre, S. Buzzi, and E. G. Larsson, “Massive MIMO in sub-6 GHz and mmWave: Physical, practical, and use-case differences,” *IEEE Wireless Communications*, vol. 26, no. 2, pp. 100–108, 2019.

[10] A. Standaert, M. Rousstia, S. Sinaga, and P. Reynaert, “Analysis and experimental verification of the HE11 mode in hollow PTFE fibers,” in *Proc. of 2015 Asia-Pacific Microwave Conference (APMC)*, vol. 3, 2015, pp. 1–3.

[11] M. De Wit, Y. Zhang, and P. Reynaert, “Analysis and design of a foam-cladded PMF link with phase tuning in 28-nm CMOS,” *IEEE Journal of solid-state circuits*, vol. 54, no. 7, pp. 1960–1969, 2019.

[12] P. Reynaert, M. Tytgat, W. Volkaerts, A. Standaert, Y. Zhang, M. De Wit, and N. Van Thienen, “Polymer microwave fibers: a blend of RF, copper and optical communication,” in *Proc. of ESSCIRC Conference 2016: 42nd European Solid-State Circuits Conference*, 2016, pp. 15–20.

[13] F. Strömbeck, “Integrated Circuit Design for High Data Rate Polymer Microwave Fiber Communication,” 2023, Doctoral thesis. [Online]. Available: <https://research.chalmers.se/en/publication/534754>

[14] M. Sarajlić, N. Tervo, A. Pärssinen, L. H. Nguyen, H. Halbauer, K. Roth, V. Kumar, T. Svensson, A. Nimr, S. Zeitz, M. Dörpinghaus, and G. Fettweis, “Waveforms for sub-THz 6G: Design guidelines,” in *Proc. of 2023 Joint European Conference on Networks and Communications & 6G Summit (EuCNC/6G Summit)*, 2023, pp. 168–173.

[15] J. Beas, G. Castanon, I. Aldaya, A. Aragon-Zavala, and G. Campuzano, “Millimeter-wave frequency radio over fiber systems: A survey,” *IEEE Communications Surveys & Tutorials*, vol. 15, no. 4, pp. 1593–1619, 2013.

[16] M. Sung, S. Kim, E.-S. Kim, S.-R. Moon, M. Kim, I.-M. Lee, K. H. Park, J. Ki Lee, and S.-H. Cho, “Design of RoF-based fiber-wireless system for THz-band 6G indoor network,” in *Proc. of 2022 European Conference on Optical Communication (ECOC)*, 2022, pp. 1–4.

[17] J. Riepl, J. Raab, P. Abajyan, H. Nong, J. Freeman, L. Li, E. H. Linfield, A. G. Davies, A. Wacker, T. Albes *et al.*, “Field-resolved high-order sub-cycle nonlinearities in a Terahertz semiconductor laser,” *Light: Science & Applications*, vol. 10, no. 1, p. 246, 2021.

[18] L. Jia, J. Wu, Y. Zhang, Y. Qu, B. Jia, and D. J. Moss, “Third-order optical nonlinearities of 2D materials at telecommunications wavelengths,” *Micromachines*, vol. 14, no. 2, p. 307, 2023.

[19] H. Q. Ngo, G. Interdonato, E. G. Larsson, G. Caire, and J. G. Andrews, “Ultradense Cell-Free Massive MIMO for 6G: Technical overview and open questions,” *Proceedings of the IEEE*, pp. 1–27, 2024.

[20] F. Conceição, A. Pereira, M. Gomese, V. Silva, and R. Dinis, “Active intelligent surfaces for next generation radio systems: An overview on large intelligent surfaces and radio stripes,” in *Proc. of 14th International Symposium on Communication Systems, Networks and Digital Signal Processing (CSNDSP)*, 2024, pp. 477–482.

[21] A. Fascista, B. J. B. Deutschmann, M. F. Keskin, T. Wilding, A. Coluccia, K. Witrisal, E. Leitinger, G. Seco-Granados, and H. Wymeersch, “Uplink joint positioning and synchronization in Cell-Free deployments with radio stripes,” in *Proc. of IEEE International Conference on Communications Workshops (ICC Workshops)*, 2023, pp. 1330–1336.

[22] S. R. Aghdam, S. Jacobsson, U. Gustavsson, G. Durisi, C. Studer, and T. Eriksson, “Distortion-aware linear precoding for massive MIMO downlink systems with nonlinear power amplifiers,” *arXiv preprint arXiv:2012.13337*, 2020.

[23] M. Majidi, A. Mohammadi, and A. Abdipour, “Analysis of the power amplifier nonlinearity on the power allocation in cognitive radio networks,” *IEEE Transactions on Communications*, vol. 62, no. 2, pp. 467–477, 2014.

[24] 3GPP, “Study on new radio access technology: Radio access architecture and interfaces,” 3rd Generation Partnership Project (3GPP), Technical Report TR 38.901, 2017, release 17. [Online]. Available: [https://www.etsi.org/deliver/etsi\\_tr/138900\\_138999/138901/17.01.00\\_60/tr\\_138901v170100p.pdf](https://www.etsi.org/deliver/etsi_tr/138900_138999/138901/17.01.00_60/tr_138901v170100p.pdf)

## APPENDIX

In this appendix, we provide the detailed derivations of the CRLB shown in Section V. Specifically, we write the respective derivations of the CRLB for both the flat-fiber and frequency-selective fiber assumptions. Note that both CRLBs are obtained from (11). The two types of fiber show different characteristics. Hence, we present the CRLB for each case separately. We define  $\Omega_k \triangleq \phi + r\psi_k - 2\pi f_k \tau$ .

### CRLB FOR FLAT FIBER

$$[\mathbf{I}(\theta)]_{|A|,|A|} = 2\Re \left\{ \frac{G^{(2r+2)}}{(r+1)\sigma^2} \sum_{k=0}^{K-1} |H_k|^{2r} |s_k|^2 e^{-j(\Omega_k)} e^{j(\Omega_k)} \right\},$$

$$= 2 \frac{G^2}{(r+1)\sigma^2} \sum_{k=0}^{K-1} |s_k|^2, \quad (42a)$$

$$[\mathbf{I}(\theta)]_{|A|,\phi} = 2\Re \left\{ \frac{j|A|G^2}{(r+1)\sigma^2} \sum_{k=0}^{K-1} |s_k|^2 e^{-j(\Omega_k)} e^{j(\Omega_k)} \right\},$$

$$= 0, \quad (42b)$$

$$[\mathbf{I}(\theta)]_{|A|,\tau} = 2\Re \left\{ -\frac{j2\pi G^2 |A|}{(r+1)\sigma^2} \sum_{k=0}^{K-1} f_k |s_k|^2 e^{-j(\Omega_k)} e^{j(\Omega_k)} \right\},$$

$$= 0, \quad (42c)$$

$$[\mathbf{I}(\theta)]_{|A|,r} = 2\Re \left\{ \frac{G^2 |A|}{(r+1)\sigma^2} \sum_{k=0}^{K-1} |s_k|^2 (j\psi_k) \right\},$$

$$= 0, \quad (42d)$$

$$[\mathbf{I}(\theta)]_{\phi,\phi} = 2\Re \left\{ \frac{-j^2 |A|^2 G^2}{(r+1)\sigma^2} \sum_{k=0}^{K-1} |s_k|^2 e^{-j(\Omega_k)} e^{j(\Omega_k)} \right\},$$

$$= 2 \frac{G^2 |A|^2}{(r+1)\sigma^2} \sum_{k=0}^{K-1} |s_k|^2, \quad (42e)$$

$$[\mathbf{I}(\theta)]_{\phi,\tau} = 2\Re \left\{ \frac{j^2 2\pi |A|^2 G^2}{(r+1)\sigma^2} \sum_{k=0}^{K-1} f_k |s_k|^2 e^{-j(\Omega_k)} e^{j(\Omega_k)} \right\},$$

$$= - \frac{4\pi G^2 |A|^2}{(r+1)\sigma^2} \sum_{k=0}^{K-1} f_k |s_k|^2, \quad (42f)$$

$$[\mathbf{I}(\theta)]_{\phi,r} = 2\Re \left\{ \frac{-j |A|^2 G^2}{(r+1)\sigma^2} \sum_{k=0}^{K-1} |s_k|^2 (j\psi_k) \right\},$$

$$= 2 \frac{G^2 |A|^2}{(r+1)\sigma^2} \sum_{k=0}^{K-1} |s_k|^2 \psi_k, \quad (42g)$$

$$[\mathbf{I}(\theta)]_{\tau,\tau} = 2\Re \left\{ \frac{-j^2 4\pi^2 |A|^2 G^2}{(r+1)\sigma^2} \sum_{k=0}^{K-1} f_k^2 |s_k|^2 e^{-j(\Omega_k)} e^{j(\Omega_k)} \right\},$$

$$= \frac{8\pi^2 G^2 |A|^2}{(r+1)\sigma^2} \sum_{k=0}^{K-1} f_k^2 |s_k|^2, \quad (42h)$$

$$[\mathbf{I}(\theta)]_{r,r} = K \left\{ \frac{\sigma^2}{(r+1)\sigma^2} \frac{\sigma^2}{(r+1)\sigma^2} \right\}$$

$$+ 2\Re \left\{ \frac{|A|^2 G^2}{(r+1)\sigma^2} \sum_{k=0}^{K-1} |s_k|^2 (-j\psi_k) (j\psi_k) \right\},$$

$$= \frac{K}{(r+1)^2} + 2 \frac{G^2 |A|^2}{(r+1)\sigma^2} \sum_{k=0}^{K-1} |s_k|^2 \psi_k^2, \quad (42i)$$

$$[\mathbf{I}(\theta)]_{\tau,r} = 2\Re \left\{ \frac{j2\pi |A|^2 G^2}{(r+1)\sigma^2} \sum_{k=0}^{K-1} f_k |s_k|^2 (j\psi_k) \right\},$$

$$= - \frac{4\pi G^2 |A|^2}{(r+1)\sigma^2} \sum_{k=0}^{K-1} |s_k|^2 f_k \psi_k. \quad (42j)$$

### CRLB FOR FREQUENCY SELECTIVE FIBER

$$[\mathbf{I}(\theta)]_{|A|,|A|} = 2\Re \left\{ G^2 \sum_{k=0}^{K-1} \frac{(b_k - 1) b_k^r |s_k|^2 e^{-j(\Omega_k)} e^{j(\Omega_k)}}{\sigma^2 (b_k^{r+1} - 1)} \right\},$$

$$= 2G^2 \sum_{k=0}^{K-1} \frac{(b_k - 1) b_k^r |s_k|^2}{\sigma^2 (b_k^{r+1} - 1)}, \quad (43a)$$

$$[\mathbf{I}(\theta)]_{|A|,\phi} = 2\Re \left\{ j|A|G^2 \sum_{k=0}^{K-1} \frac{(b_k - 1) b_k^r |s_k|^2 e^{-j(\Omega_k)} e^{j(\Omega_k)}}{\sigma^2 (b_k^{r+1} - 1)} \right\},$$

$$= 0, \quad (43b)$$

$$[\mathbf{I}(\theta)]_{|A|,\tau} = 2\Re \left\{ -j2\pi G^2 |A| \sum_{k=0}^{K-1} \frac{(b_k - 1) f_k b_k^r |s_k|^2 e^{-j(\Omega_k)} e^{j(\Omega_k)}}{\sigma^2 (b_k^{r+1} - 1)} \right\},$$

$$= 0, \quad (43c)$$

$$[\mathbf{I}(\theta)]_{|A|,r} = 2\Re \left\{ G^2 |A| \sum_{k=0}^{K-1} \frac{(b_k - 1) b_k^r |s_k|^2 (\ln |GH_k| + j\psi_k)}{\sigma^2 (b_k^{r+1} - 1)} \right\},$$

$$= 2G^2 |A| \sum_{k=0}^{K-1} \frac{(b_k - 1) b_k^r |s_k|^2 \ln \sqrt{b_k}}{\sigma^2 (b_k^{r+1} - 1)}, \quad (43d)$$

$$[\mathbf{I}(\theta)]_{\phi,\phi} = 2\Re \left\{ |A|^2 G^2 \sum_{k=0}^{K-1} \frac{(b_k - 1) b_k^r |s_k|^2 e^{-j(\Omega_k)} e^{j(\Omega_k)}}{\sigma^2 (b_k^{r+1} - 1)} \right\},$$

$$= 2G^2 |A|^2 \sum_{k=0}^{K-1} \frac{(b_k - 1) b_k^r |s_k|^2}{\sigma^2 (b_k^{r+1} - 1)}, \quad (43e)$$

$$[\mathbf{I}(\theta)]_{\phi,\tau} = 2\Re \left\{ -2\pi |A|^2 G^2 \sum_{k=0}^{K-1} \frac{(b_k - 1) f_k b_k^r |s_k|^2 e^{-j(\Omega_k)} e^{j(\Omega_k)}}{\sigma^2 (b_k^{r+1} - 1)} \right\},$$

$$= -4\pi G^2 |A|^2 \sum_{k=0}^{K-1} \frac{(b_k - 1) f_k b_k^r |s_k|^2}{\sigma^2 (b_k^{r+1} - 1)}, \quad (43f)$$

$$[\mathbf{I}(\theta)]_{\phi,r} = 2\Re \left\{ -j |A|^2 G^2 \sum_{k=0}^{K-1} \frac{(b_k - 1) b_k^r |s_k|^2 (\ln |GH_k| + j\psi_k)}{\sigma^2 (b_k^{r+1} - 1)} \right\},$$

$$= 2G^2 |A|^2 \sum_{k=0}^{K-1} \frac{(b_k - 1) b_k^r |s_k|^2 \psi_k}{\sigma^2 (b_k^{r+1} - 1)}, \quad (43g)$$

$$[\mathbf{I}(\theta)]_{\tau,\tau} = 2\Re \left\{ 4\pi^2 |A|^2 G^2 \sum_{k=0}^{K-1} \frac{(b_k - 1) f_k^2 b_k^r |s_k|^2 e^{-j(\Omega_k)} e^{j(\Omega_k)}}{\sigma^2 (b_k^{r+1} - 1)} \right\},$$

$$= 8\pi^2 G^2 |A|^2 \sum_{k=0}^{K-1} \frac{(b_k - 1) f_k^2 b_k^r |s_k|^2}{\sigma^2 (b_k^{r+1} - 1)}, \quad (43h)$$

$$\begin{aligned}
[\mathbf{I}(\theta)]_{r,r} &= \text{tr} \left\{ \mathbf{C}(\boldsymbol{\theta})^{-1} \frac{\partial \mathbf{C}(\boldsymbol{\theta})}{\partial r} \mathbf{C}(\boldsymbol{\theta})^{-1} \frac{\partial \mathbf{C}(\boldsymbol{\theta})}{\partial r} \right\} + 2\Re \left\{ |A|^2 G^2 \sum_{k=0}^{K-1} \frac{(b_k - 1)|s_k|^2 b_k^r (\ln |GH_k| - j\psi_k) (\ln |GH_k| + j\psi_k)}{\sigma^2(b_k^{r+1} - 1)} \right\}, \\
&= \sum_{k=0}^{K-1} \left( \frac{b_k^r \ln b_k}{1 - b_k^{r+1}} \right)^2 + 2G^2 |A|^2 \sum_{k=0}^{K-1} \frac{|s_k|^2 (b_k - 1) b_k^r ((\ln \sqrt{b_k})^2 + \psi_k^2)}{\sigma^2(b_k^{r+1} - 1)}, \tag{43i}
\end{aligned}$$

$$\begin{aligned}
[\mathbf{I}(\theta)]_{\tau,r} &= 2\Re \left\{ j2\pi |A|^2 G^2 \sum_{k=0}^{K-1} \frac{(b_k - 1) f_k b_k^r |s_k|^2 (\ln |GH_k| + j\psi_k)}{\sigma^2(b_k^{r+1} - 1)} \right\}, \\
&= -4\pi G^2 |A|^2 \sum_{k=0}^{K-1} \frac{(b_k - 1) b_k^r |s_k|^2 f_k \psi_k}{\sigma^2(b_k^{r+1} - 1)}. \tag{43j}
\end{aligned}$$